ADVANCED HEALTHCARE MATERIALS
www.advhealthmat.de

Dual Antibiotics-Based pH-Responsive Carrier-Free Nanodrug against Bacterial Mixed Infection for Accelerated Wound Healing

Jiali Yang, Xiaoyu Zhang, Yanan Fu, Guofeng Li, Wensheng Xie,* and Xing Wang**

Mixed infections caused by multiple bacteria are a key challenge hindering wound healing in the field of trauma care. Although antibiotics have exhibited efficient therapeutic efficacy, it is difficult for a single antibiotic to exert synergistic bactericidal effects against both Gram-positive (G^+) and Gram-negative (G^-) bacteria in mixed infection. Meanwhile, long-term treatment in high doses is prone to induce drug toxicity and accelerate the emergence of drug-resistance. Therefore, in this study, polymyxin B (PMB, targeting G^- bacteria) and bornyl *p*-aldehyde benzoate (BF, targeting G^+ bacteria) are introduced to construct pH-responsive carrier-free nanodrug (PBN) via a molecular self-assembly strategy based on dynamic Schiff-base bonding. Once triggered by the acidic microenvironment in infection site, PBN can specifically release PMB and BF synchronously through Schiff-base bond breaking, which then targeting and killing multidrug-resistant *Pseudomonas aeruginosa* (MDR-PA) and *Staphylococcus aureus* (MDR-SA), respectively. Compared with PMB/BF dual-drug administration, PBN presents higher efficiency for disrupting the membrane integrity of mixed infection. Furthermore, in vivo experiments confirm that PBNs can efficiently eliminate bacterial mixed infection to accelerate wound healing. Considering the good biosafety, the carrier-free self-assemble strategy based on different antibiotics provides an innovative route for the treatment of bacterial mixed infections.

1. Introduction

Bacterial infections pose a substantial threat to global public health, exhibiting the capacity to invade diverse anatomical systems, which ranging from cutaneous tissues to the central nervous system.[1,2] Notably, bacterial mixed infections represent a critical clinical challenge, as they complicate therapeutic management in pathologies such as diabetic foot ulcers, cystic fibrosis-related pulmonary infections, and chronic osteomyelitis.[3–5] For example, diabetic foot ulcers often experience delayed wound healing due to mixed infections, which also increases the risk of amputation. Meanwhile, in cystic fibrosis-related pulmonary infections, the mucus layer hinders drug penetration. These infections are frequently complicated by synergistic bacterial mixed interactions between Gram-positive (G^+) and Gram-genitive (G^-) bacterium, which demonstrate divergent antibiotic susceptibility patterns.[6,7] Contemporary therapeutic strategies frequently employ combination antibiotic regimens to broaden antibacterial coverage. However, the clinical utility of these approaches is often limited by multifactorial challenges, including elevated dosage requirements, spatiotemporal heterogeneity in drug distribution, and the risk of pharmacodynamic antagonism between agents.[8,9] These limitations are further compounded by the inherent physicochemical constraints of conventional antibiotics—such as suboptimal aqueous solubility, restricted tissue biodistribution, and rapid renal clearance—as well as the escalating global burden of multidrug resistance (MDR). Collectively, these factors contribute to suboptimal patient outcomes and necessitate the development of novel therapeutic paradigms to address the evolving complexity of bacterial mixed infections.[10,11]

Nanoparticle-mediated drug delivery systems have emerged as a paradigm-shifting therapeutic strategy to enhance the efficacy of antibacterial interventions. Engineered nanocarriers-such as liposomal vesicles and polymeric matrices-offer multifunctional advantages, including enhanced pharmacokinetic profiles, superior tissue permeation capabilities, and the ability to evade microbial resistance mechanisms through stealth functionalization.[12–14] Nevertheless, conventional nanodelivery platforms remain limited by intrinsic limitations, such as suboptimal drug-loading capacities, complex multi-step synthesis protocols, and persistent biocompatibility challenges arising from carrier material accumulation in vivo.[15,16] To address these shortcomings, carrier-free nanodrug delivery systems have

J. Yang, X. Zhang, Y. Fu, G. Li, W. Xie, X. Wang
State Key Laboratory of Organic-Inorganic Composites
College of Life Science and Technology
Beijing University of Chemical Technology
Beijing 100029, China
E-mail: ligf@mail.buct.edu.cn; xws@mail.buct.edu.cn; wangxing@mail.buct.edu.cn
J. Yang, X. Zhang, Y. Fu, G. Li, W. Xie, X. Wang
Beijing Laboratory of Biomedical Materials
Beijing University of Chemical Technology
Beijing 100029, China

The ORCID identification number(s) for the author(s) of this article can be found under https://doi.org/10.1002/adhm.202501845

DOI: 10.1002/adhm.202501845

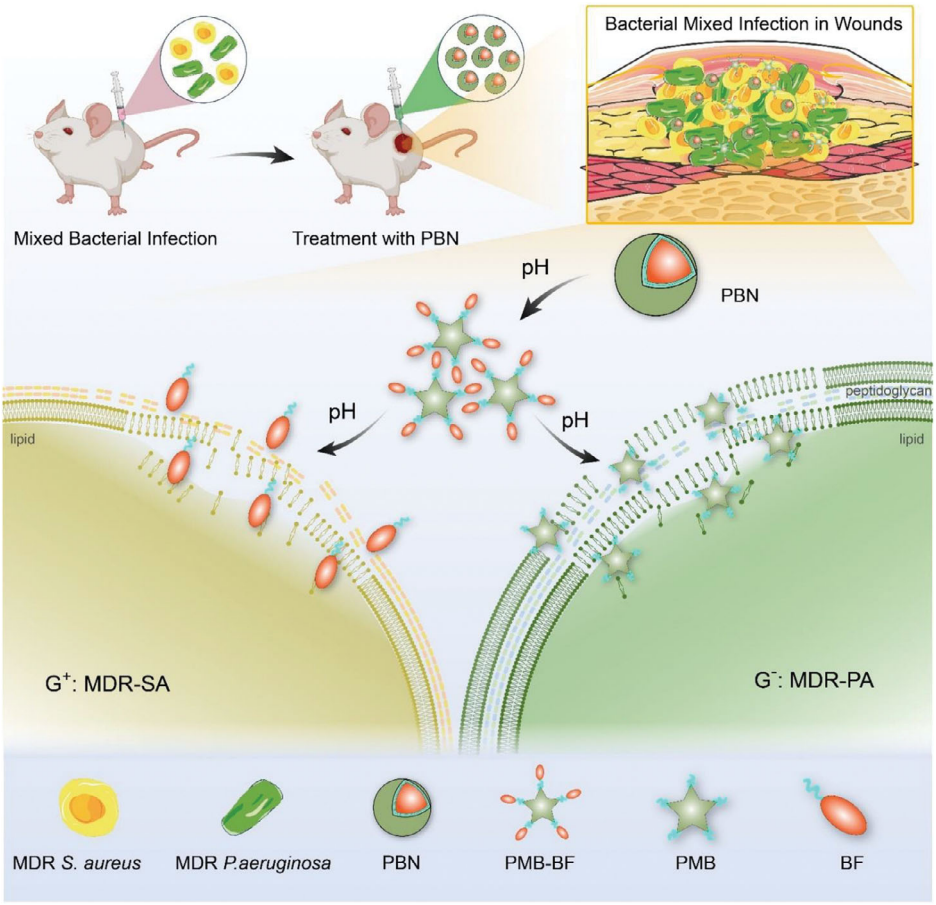

Scheme 1. Schematic illustration of PBN against bacterial mixed infection (MDR *S. aureus* and MDR *P.aeruginosa*) for accelerated wound healing. Once penetrating into the wound tissue, acidic environment triggers deconstruction of PBN and releasing of PMB and BF. The combination PMB (interfering with lipids) and BF (interfering with peptidoglycan) by PBN successfully induces the cytolysis of both G^+ (MDR-SA) and G^- (MDR-PA) bacteria in mixed infection.

gained significant attention as a disruptive innovation in antibacterial pharmacology.[17] These systems leverage supramolecular co-assembly of pharmacologically active agents into discrete nanostructures, achieving near-quantitative drug encapsulation efficiencies (>90% w/w) while eliminating reliance on inert excipients. This carrier-free paradigm not only addresses physicochemical limitations by enhancing aqueous solubility, colloidal stability, and site-specific biodistribution,[18] but also enables spatiotemporally coordinated co-delivery of combinatorial therapeutics to pathological microenvironments. Such precision targeting potentiates synergistic therapeutic outcomes through simultaneous drug activation, thereby optimizing pharmacodynamic profiles and mitigating off-target cytotoxicity.[19] The active compound borneol, found in medicinal plants, exhibits bactericidal and anti-inflammatory effects.[20] In our previous research, its esterified derivative (BF) can effectively eliminate multidrug-resistant *staphylococcus aureus* (MDR-SA). Polymyxin B (PMB), on the other hand, is a poly-amino cyclic cationic polypeptide that can effectively combat G^- bacteria.[21]

In this study, PMB (targeting G^- bacteria) and bornyl p-aldehyde benzoate (BF, targeting G^+ bacteria) were introduced to construct a pH-responsive carrier-free nanodrug (PBN) via a molecular self-assembly strategy based on the dynamic Schiff-base bonding (**Scheme 1**). Once triggered by the acidic microenvironment at the infection site, PBN can specifically release PMB and BF synchronously through Schiff-base bond cleavage, thereby targeting and killing multidrug-resistant *P. aeruginosa* (MDR-PA) and MDR-SA, respectively. Compared with dual-drug administration of PMB and BF, PBN presents higher efficiency for disrupting the membrane integrity of mixed infections. Furthermore, both in vitro and in vivo evaluations confirmed the outstanding capacity of PBN for eradicating bacterial mixed infection and accelerating wound healing. Considering the biocompatibility, this carrier-free self-assembly strategy based on two antibiotics offers an innovative approach for treating bacterial mixed infections in trauma care.

2. Results and Discussion

2.1. Preparation of PBN and Characterization

The carrier-free nanodrug PBN was prepared using an oil-water emulsion template method. In this process, the hydrophobic

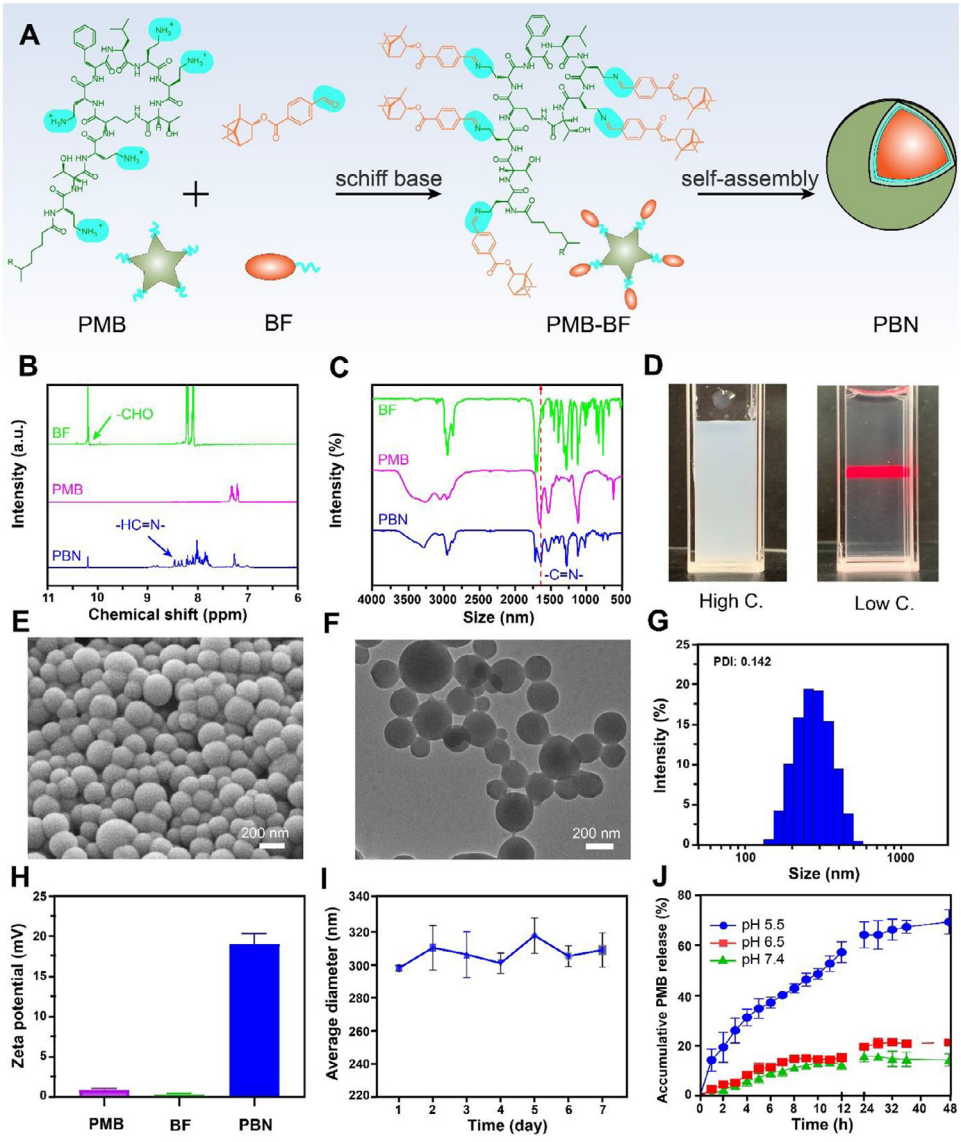

Figure 1. Preparation and characterization of PBN. A) Schematic illustration of preparation process for PBN; B) ^{1}H-NMR analysis of BF, PMB, and PBN; C) FT-IR spectra of BF, PMB, and PBN; D) Tyndall effect of PBN in aqueous solution with different concentration; E) SEM image of PBN; F) TEM image of PBN; G) Particle size distribution of PBN by DLS analysis; H) Surface charge of PBN in aqueous solution, *N*=3; I) Particle size of PBN in aqueous solution for 7 days, *N*=3; J) Accumulative release profile of PMB from PBN under different pH buffers (5.5, 6.5, 7.4), *N*=3.

compound BF (Figure S1, Supporting Information) was dissolved in the oil phase, while the hydrophilic antibiotic PMB was dispersed in the aqueous phase. At the oil-water interface, BF's aldehyde groups reacted with PMB's amino groups via Schiff-base formation, yielding an amphiphilic conjugate. This conjugate subsequently self-assembled through hydrophilic-hydrophilic interactions, resulting in the formation of PBN nanoparticles (**Figure** 1A). Proton nuclear magnetic resonance (^{1}H NMR) spectroscopy of PBN exhibited a characteristic -C═N- chemical shift between δ 9.23 and 10.00 ppm (Figure 1B). Meanwhile, free -CHO from BF were also detected in PBN due to incomplete reaction. The mass ratio of PMB to BF in the formulation was determined to be 4:6 (w/w) (Table S1, Supporting Information). Fourier-transform infrared (FT-IR) spectroscopy of PBN revealed a distinctive imine (-C═N) absorption peak at 1640 cm^{-1} compared to PMB and BF, confirming the successful Schiff-base formation between BF and PMB (Figure 1C).[22] A concentrated PBN dispersion in deionized water exhibited an emulsion-like appearance and displayed a distinct Tyndall effect upon dilution (Figure 1D), demonstrating the self-assembled nanostructure. Scanning electron microscopy (SEM) and transmission electron microscopy (TEM) images demonstrated that PBN nanoparticles possessed a regular, solid spherical morphology with diameters ranging from 200 to 300 nm (Figure 1E,F). Dynamic light scattering (DLS) measurements corroborated these findings, indicating a hydrated particle size within the same range (≈300 nm) and a polydispersity index (PDI) of 0.142 (Figure 1G). Zeta potential analysis revealed a positive surface charge of +17.1 ± 1.1

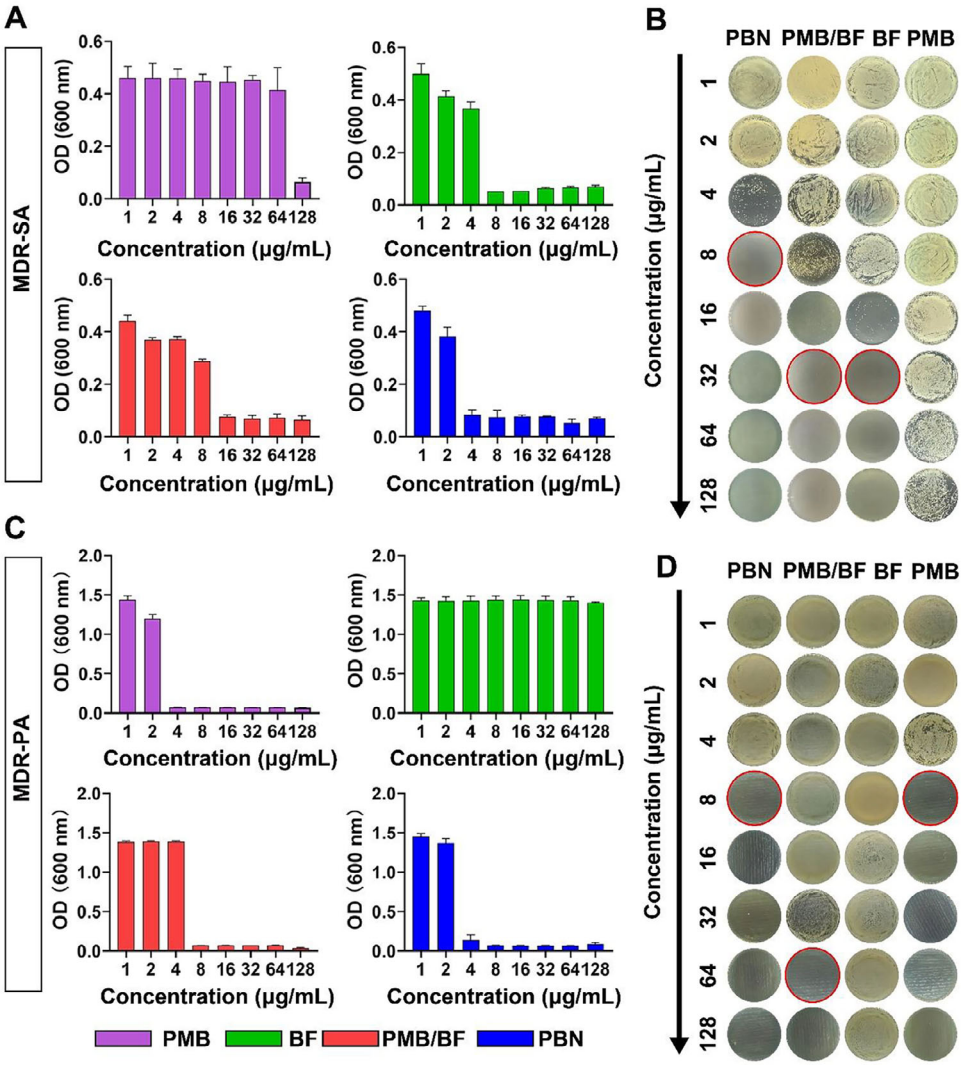

Figure 2. Evaluation of in vitro antibacterial activity of PBN on MDR-SA or MDR-PA model. A) MIC assay of PMB, BF, PMB/BF, and PBN co-incubated with MDR-SA, *N*=3; B) MBC assay of PMB, BF, PMB/BF, and PBN co-incubated with MDR-SA; C) MIC assay of PMB, BF, PMB/BF, and PBN co-incubated with MDR-PA, *N*=3; D) MBC assay of PMB, BF, PMB/BF, and PBN.

mV (Figure 1H), suggesting that PBN could effectively interact with negatively charged bacterial surfaces through electrostatic attraction.[23,24] PBN exhibited notable stability in phosphate-buffered saline (PBS) at pH 7.4 over a seven-day period, maintaining an average particle size of ≈ 300 nm without observable precipitation or aggregation (Figure 1I). Cumulative drug release exhibits that only less 20% of PMB was released from PBN over 48 h under pH 7.4 and 6.5 conditions, confirming the stable self-assemble structure of PBN. However, under more acidic conditions (pH 5.5), 57.4% of PMB was released within 12 h with cumulative release reaching 69.5% at 48 h (Figure 1J), as measured and calculated according to the standard curve (Figure S2, Supporting Information). This pH-responsive release behavior is attributed to the acid-sensitive nature of the Schiff-base linkage, which undergoes hydrolysis in acidic environments.[25] These unique advantages suggest that PBN can effectively release its therapeutic payloads in the acidic microenvironment of infected tissues, thereby minimizing premature drug leakage and reducing potential systemic toxicity.

2.2. Antibacterial Performance of PBN against MDR-SA and MDR-PA

As the BF and PMB components of PBN are sensitive to G^- and G^+ bacteria respectively, MDR-SA and MDR-PA were used as models to assess the antibacterial efficacy of PBN against mixed infections. As shown in **Figure** 2A, the minimum inhibitory concentration (MIC) for MDR-SA was determined to be 8 μg mL^{-1} for BF, 128 μg mL^{-1} for PMB, and 16 μg mL^{-1} for the physical mixture of PMB and BF (PMB/BF, consisting of 6.4 μg mL^{-1} BF and 9.6 μg mL^{-1} PMB). It is evident that BF is more effective against MDR-SA compared to PMB. Notably, the MIC of PBN against MDR-SA was reduced to 4 μg mL^{-1}, rep-

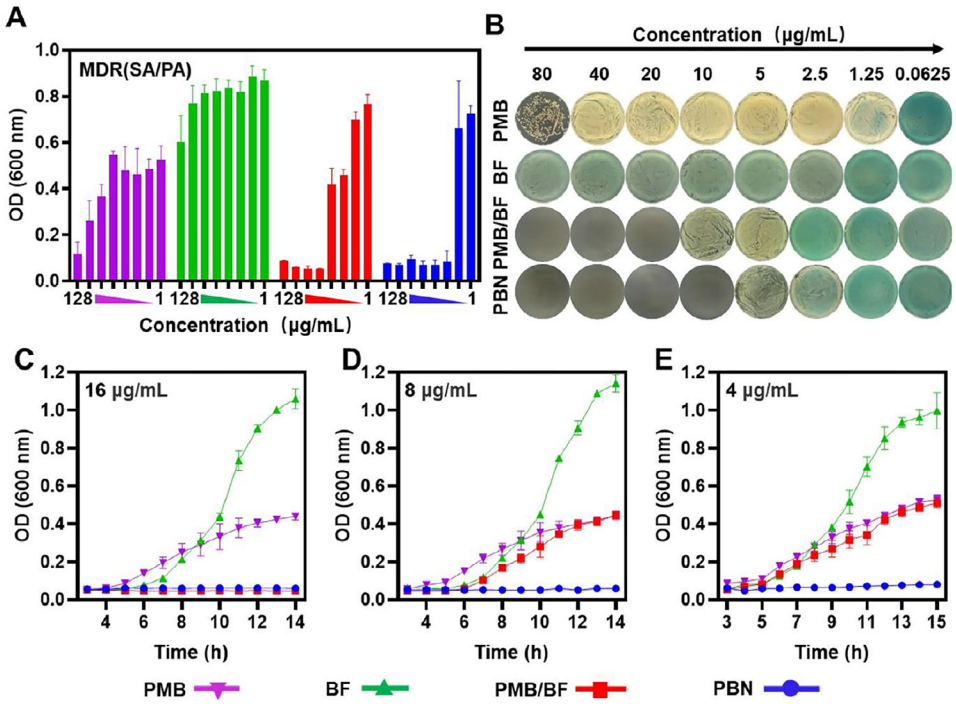

Figure 3. In vitro evaluation of antibacterial activity of PBN under the co-mixture model of MDR-SA and MDR-PA. A) MIC assay of PMB, BF, PMB/BF, and PBN co-incubated with MDR (SA/PA), *N*=3; B) MBC assay of PMB, BF, PMB/BF, and PBN co-incubated with MDR (SA/PA); C–E) Growth curves of different concentrations of PMB, BF, PMB/BF, and PBN co-incubated with MDR (SA/PA), *N*=3.

resenting a 4-fold decrease compared to PMB/BF. These findings suggest that the self-assembled nanostructure contributes to the antibacterial effect with BF as the primary contributor. The minimum bactericidal concentration (MBC) against MDR-SA (Figure 2B) was >128 μg mL^{-1} for PMB, 32 μg mL^{-1} for BF, 32 μg mL^{-1} for PMB/BF, and 8 μg mL^{-1} for PBN. This indicates a fourfold reduction in the MBC of PBN compared to free BF alone. These results indicate that the carrier-free nanodrug PBN not only preserves the antibacterial activity of BF against MDR-SA but also effectively reduces the required drug dosage, potentially mitigating adverse effects associated with high-dose administration.[26]

In contrast, the MIC for PMB, BF, PMB/BF, and PBN for G$^-$ MDR-PA was about 4, >128, 8, and 4 μg mL^{-1}, respectively (Figure 2C). Notably, the antibacterial activity of PBN is primarily attributed to the PMB component. More importantly, PBN showed a lower MIC value (4 μg mL^{-1}) compared to PMB/BF (8 μg mL^{-1}), which is agreement with the results on G$^+$ MDR-SA. Additionally, the MBC of PBN (8 μg mL^{-1}) was 8-fold lower than that of PMB/BF (64 μg mL^{-1}) (Figure 2D). These findings confirm that the nanoparticle formulation effectively reduces the required antibacterial dosage of PMB against MDR-PA. Collectively, the results demonstrate that PBN retains the efficacy of BF against G$^+$ bacteria and that of PMB against G$^-$ bacteria regardless of the Schiff-base reaction. Notably, the self-assembled nanostructure of PBN further enhance the antibacterial performance of PMB and BF to G$^-$ and G$^+$ bacteria respectively, suggesting potential advantages for treating bacterial mixed infections.

2.3. In Vitro Antibacterial Activity for Bacterial Mixed Infections

In an effort to evaluate the efficacy of PBN in eradicating bacterial mixed infections, a model comprising equal volumes of MDR-SA and MDR-PA was employed. The MIC assay results (**Figure** 3A) demonstrated that both PMB/BF and PBN exhibited significantly greater antibacterial activity compared to PMB or BF alone. The MIC for MDR(SA/PA) of PMB/BF and PBN was ≈ 16 and 4 μg mL^{-1}, respectively. PBN exhibited a 4-fold decrease in MIC relative to the PMB/BF, suggesting the advantages of PBN for effectively inhibiting the growth of both G$^+$/G$^-$ bacterial strains at lower concentrations. Furthermore, the MBC measurements underscored the enhanced bactericidal performance of PBN in eliminating the mixed bacterial population compared to PMB, BF, and PMB/BF (Figure 3B). Specifically, PBN eradicated all mixed bacteria at a concentration of 10 μg mL^{-1}, representing a 2-fold improvement in bactericidal activity compared to the PMB/BF combination (20 μg mL^{-1} for similar efficacy). Conversely, although PMB and BF alone demonstrated significant inhibitory effects against single bacterial strains (Figure 2A,C), they showed no substantial bactericidal activity against the mixed MDR (SA/PA) population. Growth curve analyses of the mixed MDR(SA/PA) provided a more intuitive depiction of the antibacterial effects across different treatment groups (Figure 3C–E). At a high concentration of 16 μg mL^{-1} PBN (equivalent to 6.4 μg mL^{-1} BF and 9.6 μg mL^{-1} PMB), both PMB/BF and PBN groups demonstrated completely inhibited bacterial growth, whereas bacterial proliferation persisted in the PMB and BF groups (Figure 3C). When the PBN

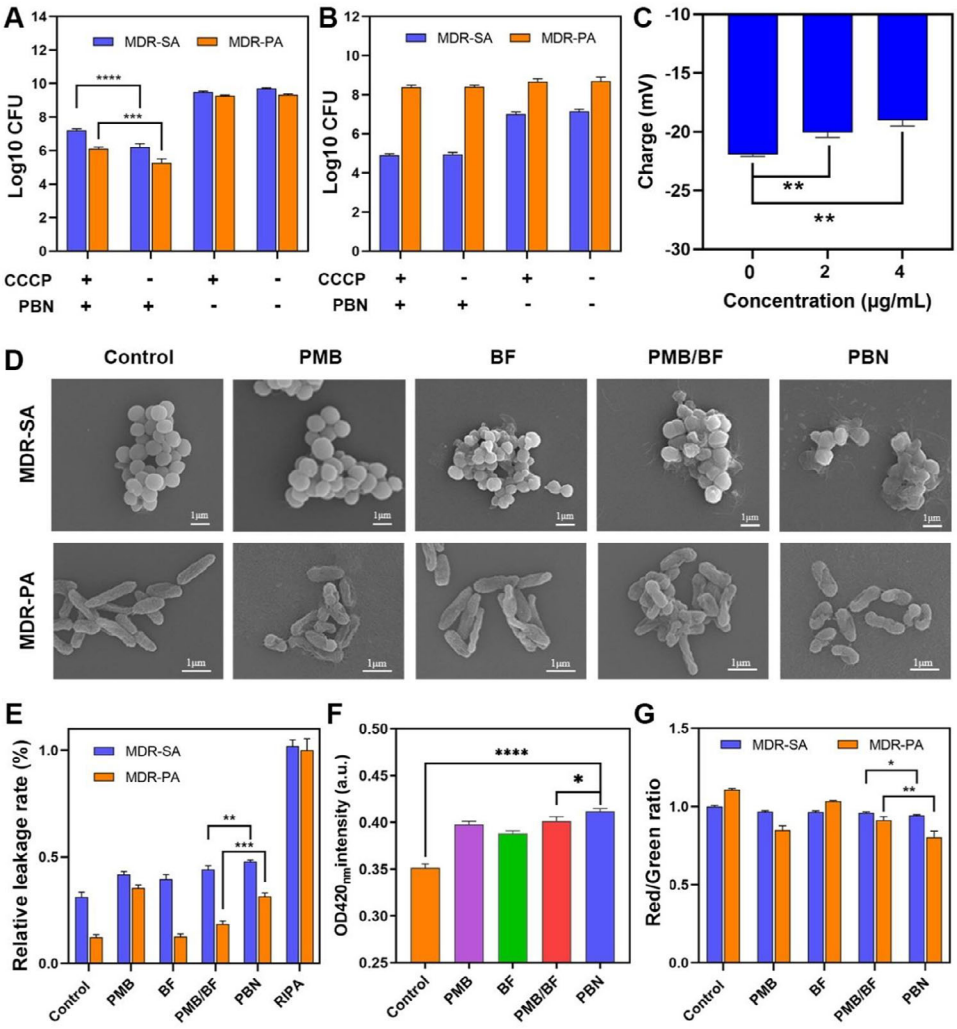

Figure 4. Antibacterial mechanism study of PBN. A) Colony counts after co-incubation of PBN with bacteria under the influence of CCCP in TSB environment, *N*=3; B) Colony counts after co-incubation of PBN with bacteria under the influence of CCCP in NaCl environment, *N*=3; C) Changes in bacterial surface charge after co-incubation of different concentrations of PBN with MDR-SA, *N*=3; D) SEM images of bacteria after 6 h of incubation with different drugs; E) Different drug treatments protein leakage rate of bacteria, *N*=3; F) Changes in membrane permeability after co-incubation of MDR-SA with different drugs, *N*=3; G) Depolarization of bacterial membrane after treatment with different drug groups, *N*=3.

concentration was reduced to 8 or 4 μg mL^{-1}, only PBN maintained a pronounced antibacterial effect, while PMB/BF failed to inhibit the growth of MDR(SA/PA) (Figure 3D,E). Notably, the inhibitory concentration of PBN for MDR(SA/PA) is consistent with the MIC values for MDR-SA and MDR-PA individually. Collectively, these results suggest that PBN not only exhibits efficient antibacterial efficacy against bacterial mixed infections, but also reduces the required drug dosage compared with physically mixed administration. This robust antibacterial activity positions PBN as a promising therapeutic candidate for the treatment of clinical bacterial mixed infections.

2.4. Antibacterial Mechanism of PBN

MDR-SA and MDR-PA depend on PMF across their cytoplasmic membranes for ATP production. Disruption of PMF impairs ATP synthesis, thereby reducing the active transport of drugs and diminishing their bactericidal efficacy. For instance, preincubation of bacteria with carbonyl cyanide m-chlorophenylhydrazone (CCCP), a protonophore that dissipates PMF, has been shown to inhibit the uptake of aminoglycosides, resulting to increased bacterial survival.[27] We preincubated MDR-SA and MDR-PA with CCCP prior to exposure to PBN. The results indicated that CCCP pretreatment led to a significant increase in bacterial colony counts compared to untreated controls in a TSB nutrient environment (**Figure** 4A), suggesting that inhibition of PMF reduced the active uptake of PBN and attenuated its antibacterial activity. In contrast, under saline conditions, CCCP did not significantly affect the bactericidal efficacy of PBN, highlighting the role of PMF in mediating PBN's effects (Figure 4B). Therefore, we hypothesize that PBN, upon entering bacterial cells via active transport mechanisms facilitated by PMF, exerts its antibacterial effects by disrupting normal metabolic processes.

As the surface membrane potential is closely related to the structural integrity of bacterial membrane,[28] the changes in

membrane potential of MDR-SA and MDR-PA during various treatments were measured. As shown in Figure 4C and Figure S3 (Supporting Information), PBN treatment significantly increased the membrane potential of both MDR-SA and MDR-PA compared to untreated ones due to the positive surface charge of PBN (+17.1 mV). Moreover, this effect intensified with increasing concentrations of co-incubated PBN. Cationic interactions with anionic sites on bacterial surfaces have been documented to disrupt bacterial physiological states.[29] The positive charge on PBN's surface enhances its adsorption onto bacterial membranes, facilitating potent bactericidal activity. The morphological changes of bacteria after different drug treatments were explored by scanning electron microscopy (Figure 4D). SEM images of MDR-SA subjected to various treatments revealed that cells treated with PBS and PMB maintained intact membranes with clear textures. In contrast, treatments with BF, PMB/BF, and PBN induced obvious membrane damage for MDR-SA. Similarly, obvious wrinkled and damaged membranes of MDR-PA were detected in PMB, PMB/BF, and PBN treatment groups compared to bacteria in the control group. This is consistent with the previous reports. The aminoglycoside antibiotic PMB exerts its bactericidal effects by disrupting the integrity of the bacterial cell membrane.[30,31] It achieves this by binding to lipid A components of the outer membrane of G^- bacteria through electrostatic interactions, leading to membrane destabilization and subsequent leakage of cellular contents by the proton motive force (PMF) process.[32,33]

Damage to bacterial membrane integrity triggers the leakage of intracellular protein into medium.[34,35] As shown in Figure 4E, quantification of protein leakage in MDR-SA and MDR-PA post-treatment showed that significantly higher protein leakage in the PBN group was detected compared to the control group, which corroborating the SEM findings. More importantly, PBN group exhibited higher protein level than PMB/BF group, demonstrating the enhanced antibacterial activity contributed by nanostructure of PBN. Additionally, o-nitrophenyl-β-galactopyranoside (ONPG) assays indicated increased membrane permeability in both the PMB/BF and PBN groups, with PBN showing a more pronounced effect (Figure 4F). DiOC2(3), a membrane potential-sensitive probe, was employed to further investigate the membrane polarization. As shown in Figure 4G, PBN treatment significantly disrupted the cell membrane potential of both MDR-SA and MDR-PA, leading to depolarization. The effects were more pronounced for PBN compared with PMB/BF, which is align with MIC and MBC data. These results reveal that PBN efficiently retains antibacterial efficacy of PMB and BF against bacteria while reducing the required administrated dosage. Collectively, these findings demonstrate that PBN's mechanism against bacteria involves electrostatic adsorption to the bacterial surface, resulting in substantial cell wall and membrane disruption, promotion of intracellular content leakage, and subsequent bacterial death.

2.5. Therapeutic Efficacy for Mixed-Bacteria Wound Infection Model

A murine skin wound infection model was employed to further investigate the efficacy of PBN in eradicating bacterial mixed infections (**Figure 5A**). Specifically, MDR-SA and MDR-PA were combined in a 1:1 ratio and introduced into murine skin wounds for 24 h, followed by in situ treatment administration (PBS, PMB, BF, PMB/BF, and PBN). Photographic documentation of the wounds was conducted on days 0, 1, 3, 5, 7, 9, and 11 across the various treatment groups (Figure 5B). At 24 h post-infection, extensive ulceration of the wounds was observed, confirming the successful establishment of the bacterial mixed infection model. After 11 days of treatment, wounds in the PBN group exhibited near-complete healing, whereas other groups displayed residual scabbing. The temporal progression of wound healing was visualized through simulation graphs depicting wound area reduction over time (Figure 5C). The PBN group demonstrated the most rapid wound closure, the smallest residual wound area, and accelerated weight gain during the recovery period (Figure 5F,G), indicating improved overall health and reduced systemic inflammation in these mice. To quantitatively assess the antibacterial activity of PBN, wound tissues from each group were collected after 11 days of treatment, homogenized, and the bacterial load was evaluated using the agar plate dilution method (Figure 5D,E). Results indicated that monotherapy groups achieved partial bacterial reduction, while the PMB/BF combination and PBN groups exhibited more substantial bacterial clearance, with the PBN group displaying the lowest bacterial burden, significantly outperforming other treatment groups. These findings substantiate that PBN effectively combats mixed bacterial wound infections in vivo and facilitates wound healing.

Histological analyses were performed to further assess tissue recovery using hematoxylin and eosin (H&E) staining and Masson's trichrome staining (Figure 5H). H&E staining revealed epithelial regeneration and epidermal thickening in the PBS, PMB, and BF groups, whereas the PMB/BF and PBN groups exhibited more advanced recovery, including regeneration of hair follicles, dermis, and other skin structures. Masson's trichrome staining assessed collagen fiber formation during the healing process,[36] demonstrating collagen deposition across all groups, with the PBN group exhibiting the most abundant collagen synthesis, significantly exceeding that of the control and other treatment groups. Additionally, the efficacy of anti-infection treatments was evaluated by measuring serum cytokine levels (IL-6, TNF-α, and IL-1β) (Figure S4, Supporting Information). The PBS group showed elevated inflammatory cytokine infiltration compared to those of normal mice, which was moderately alleviated in monotherapy and PMB/BF groups. Notably, the PBN group displayed cytokine levels comparable to normal mice, indicating effective resolution of systemic bacterial infection. Collectively, these results demonstrate that PBN possesses robust bactericidal activity, effectively promotes wound healing, and holds promise for treating mixed-bacterial wound infections.

2.6. Biosafety Measurement

Ensuring the biosafety of nanomedicines intended for in vivo therapeutic applications is paramount for their clinical translation. The in vivo biocompatibility and biosafety of PBN were assessed through cytotoxicity and hemolysis assays (**Figure 6A,B**). Free PMB and BF showed significant in vitro cytotoxicity toward Raw264.7 and L929 cells at a co-incubation concentration of ≈

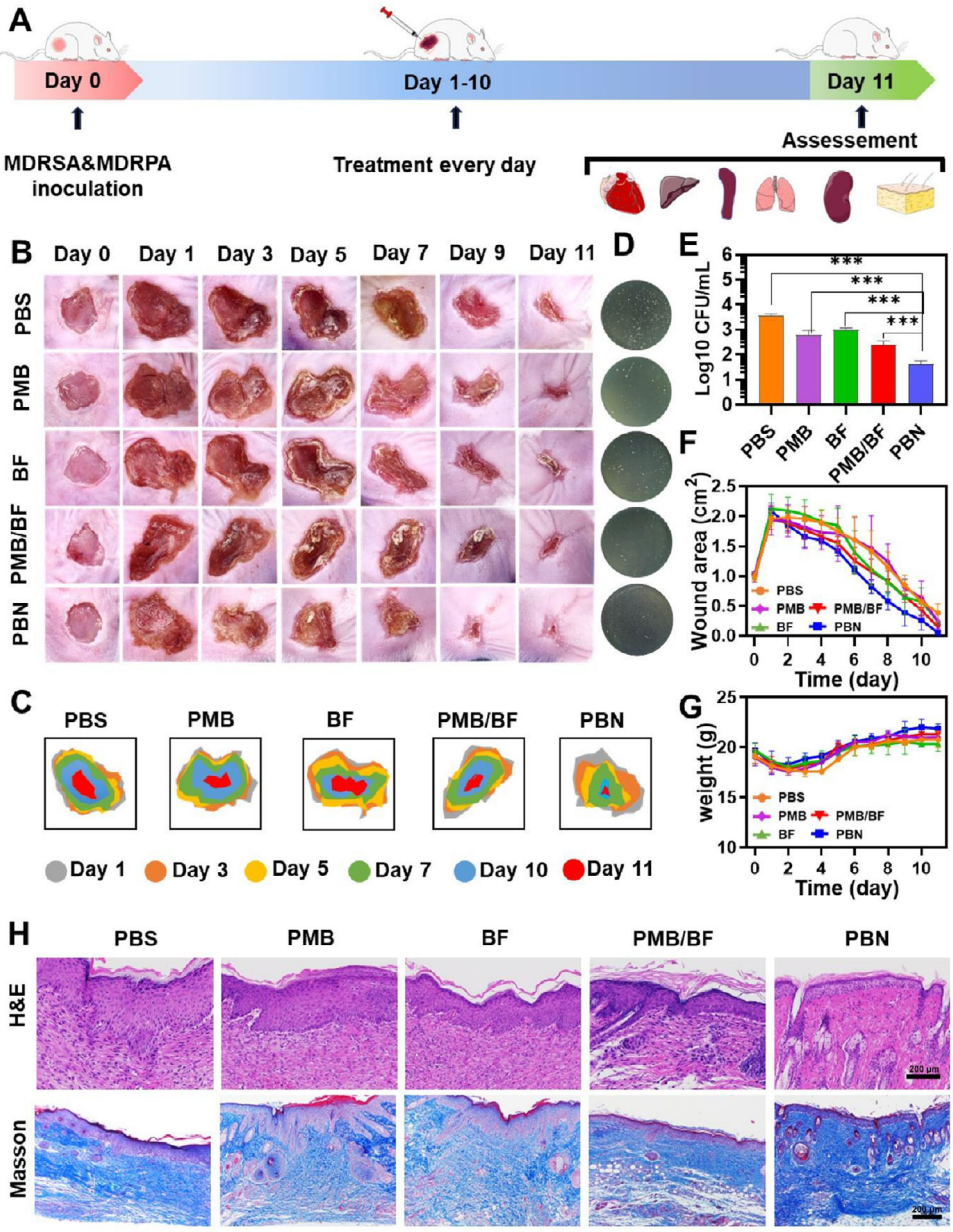

Figure 5. In vivo study of PBN for the treatment of bacterial mixed infections. A) Schematic diagram of modeling and treatment of mixed bacterial infection; B) Photographs of wounds of infected mice in each treatment group over time; C) Schematic of simulated infected skin wounds in each treatment group; D) Images of residual bacterial smears on the wounds of each treatment group on day 11; E) Count of residual bacteria (MDR(SA/PA)) on the trauma surface of each treatment group on day 11, *N*=3; F) Change curves of trauma area of mice in each treatment group, *N*=3; G) Change curve of mouse body weight in each treatment group, *N*=3; H) H&E staining and Masson staining images of skin tissues in each treatment group on day 11.

128 μg mL^{-1} (Figure S5, Supporting Information). However, the results of PBN demonstrated that the viability of both L929 and Raw264.7 cells remained above 80% even at high PBN concentrations up to 128 μg mL^{-1} (MIC of PBN is only 4 μg mL^{-1}), which greatly guarantee the biosafety requirement. Furthermore, the hemolysis rate remained substantially below 5% even at concentrations as high as 256 μg mL^{-1}, indicating negligible erythrocyte lysis (Figure 6B). These findings suggest that PBN exhibits favorable hemocompatibility, a critical factor for blood-contacting biomaterials. In addition, organ toxicity was evaluated via H&E staining of major organs (heart, liver, spleen, lung, and kidney) from treated mice. Histological analyses revealed no significant morphological abnormalities or damage in any of the examined organs across all treatment groups (Figure 6C). Both in vitro and in vivo biosafety evaluations substantiate that PBN possesses commendable biocompatibility and negligible toxicity, rendering it a promising candidate for in vivo anti-infective therapy.

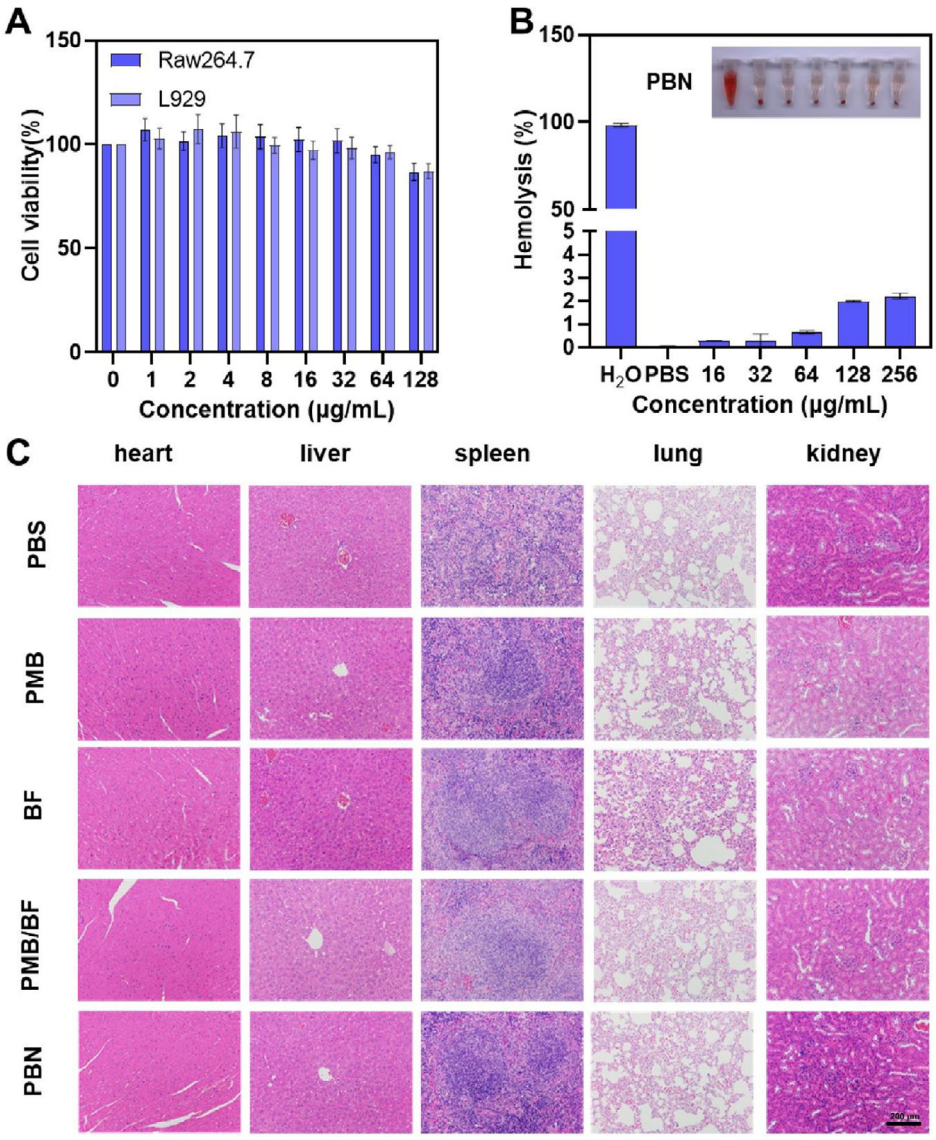

Figure 6. Biosafety evaluation of PBN. A) Relative cell viability of Raw264.7 and L929 cells after 24 h of treatment with different concentrations of PBN, *N*=3; B) Hemolysis of erythrocytes induced by different concentrations of PBN, *N*=3; C) H&E staining images of major organs of mice heart, liver, spleen, lung, and kidney in each treatment group.

3. Conclusion

In summary, a pH-responsive, carrier-free nanodrug PBN was developed through the self-assembly of two pharmacologically active agents (PMB and BF) to simultaneously eliminate bacterial mixed infection synchronously and accelerate wound healing. The nanostructured PBN adsorbs onto bacterial surfaces via electrostatic interactions, increasing the local concentration of the therapeutic agents. Then, Once triggered by the acidic microenvironment at the infection site, PBN specifically releases PMB and BF through the cleavage of Schiff-base bonds, targeting and killing MDR-PA and MDR-SA, respectively. The therapeutic mechanism against bacteria involves disruption of the cell wall and membrane, promotion of intracellular protein leakage, and subsequent bacterial death. Compared to dual-drug administration of PMB/BF, PBN demonstrates higher efficacy against bacterial mixed infections due to its self-assembled nanostructure. Furthermore, both in vitro and in vivo evaluations confirm the outstanding capacity of PBN to eradicate bacterial mixed infections and promote wound healing. Considering its biocompatibility, this carrier-free self-assembly strategy based on two antibiotics offers an innovative approach for treating bacterial mixed infections in trauma care.

4. Experimental Section

Materials: Polymyxin B (PMB, purity ≥99%) and 4-formylbenzoic acid (p-formylbenzoic acid, purity ≥97%) were purchased from Adamas Biochemical (Shanghai, China). Borneol was purchased from Abmole BioScience (Shanghai, China). Dicyclohexylcarbodiimide (DCC,

>98%) was purchased from Bioruler Biotechnology (Beijing, China). 4-dimethylaminopyridine (DMAP, HPLC grade, ≥99.5% purity) was purchased from MedChemExpress (Princeton, NJ, USA). The mouse fibroblast cell line L929 and mouse monocyte macrophage cell line RAW 264.7 were obtained from the Cell Resource Center of the Chinese Academy of Sciences (Beijing, China). Tryptic Soy Broth (TSB) and Tryptic Soy Agar (TSA) were purchased from Sinopharm Chemical Reagent (Shanghai, China). Triton X-100 surfactant and BCA protein quantification kit and carbonyl cyanide 3-chlorophenylhydrazone (CCCP) were purchased from Solarbio Life Sciences (Beijing, China). The experimental strains including methicillin-resistant *Staphylococcus aureus* (MDR-SA, CMCC 26003) were provided by the China Industrial Microbial Strain Collection and Management Center (CICC), and multidrug-resistant *Pseudomonas aeruginosa* (MDR-PA, clinical isolate PA2019) was gifted by the Clinical Microbiology Laboratory of the Sino-Japanese Friendship Hospital (CJFH), Beijing, China. 3,3'-diethyloxacarbocyanine iodide, 2-Nitrophenyl-β-D-galactopyranoside, and absolute ethanol were purchased from J&K Scientific (Beijing, China).

The Preparation of BF: Bornyl p-aldehyde benzoate (BF) was synthesized by esterification of ((1S)-endo)-(-)-borneol with p-formylbenzoic acid as follows: p-formylbenzoic acid (1.45 g, 9.658 mmol), 4-dimethylaminopyridine (0.15 g, 1.228 mmol), dicyclohexyl carbodiimide (2.60 g, 12.601 mmol), and ((1S)-endo)-(-)-borneol (1.00 g, 6.483 mmol) were added into a round-bottom flask, followed by the addition of 30 mL of anhydrous tetrahydrofuran. The reaction was kept overnight under anhydrous dry ambient conditions. The reaction product was then collected via three times filtration operations, during which it was treated with 1 mL of 50% acetic acid solution and 120 mL of ice petroleum ether. The crude product was purified by silica gel column chromatography (ethyl acetate: petroleum ether = 1:10, v/v). The chromatographic solution was dried to obtain the target product BF. The molecular structure of BF was analyzed and identified by 1H-NMR (AVANCE III, Bruker).

The Synthesis of Carrier-Free Self-Assembly Nanodrug (PBN): 24.4 µmol BF was weighed in a glass vial. Then, 1 mL of dichloromethane (CH_2Cl_2) and 3.4 mL deionized water was added to form an oil-water mixed solution. The mixed solution was stirred continuously for 4 h at a stirring speed of 1600 rpm under 37 °C. 15.3 µmol PMB was dissolved in 1.6 mL deionized water, and then slowly added dropwise to BF emulsion, and the reaction was continued for 2 h. After that, 100 µL of a 3% aqueous solution of triethylamine was added to the reaction solution, and the stirring was continued for 2 h. The precipitated product was collected and dissolved in 1 mL anhydrous ethanol and dialysis (3500 Da) in 5 mL deionized water for 48 h. After dialysis, the solution was freeze-dried to obtain PBN product.

Characterization: The size distribution and surface charge of PBN were determined using a dynamic light scattering (DLS, ZetaSizer Nano ZS90, Malvern Instruments). The PBN solution obtained by dialysis was diluted 10-fold with deionized water, and its particle size distribution and surface potential were measured by DLS. The surface morphology and structure of PBN were observed by scanning electron microscopy (SEM-7800, Hitachi) and transmission electron microscopy (TEM-7650B, Hitachi). Specifically, the PBN solution obtained by dialysis was dropped onto a conductive adhesive and a copper grid, and then dried. Subsequently, the magnification of SEM was 10,000x, and that of TEM was 40,000x. The surface chemistry reaction was measured by Fourier Transform infrared spectroscopy (FTIR, TENSOR 27). Specifically, the PBN powder obtained by dialysis and lyophilization was co-ground with KBr. After pressing into tablets, the sample was tested by FTIR.

Loading Efficiency (LE) and Encapsulation Efficiency (EE): The drug loading of PBN was determined by UV–vis spectrophotometer (UV-2450, Shanghai Yuananalytical Instrument Co., Ltd.). 2.4 mg of PMB was accurately weighed and dissolved in 2 mL of PBS with different pH values (3.0, 5.5, 6.5, and 7.4). A series of PMB standard solutions were obtained by gradient dilution of the above PMB standard solutions. The absorbance values of different concentrations of PMB standard solutions were measured at 206 nm, and the standard curve of PMB was plotted with the concentration as the horizontal coordinate and the absorbance value as the vertical coordinate. Subsequently, the PBN was placed in pH 3.0 PBS solution to destroy the structure completely, and the absorbance value of the solution was measured at 206 nm, and then the content of polymyxin B in the PBN was calculated according to the standard curve of PMB, and then the loading and encapsulation efficiency of the PBN were calculated according to the following formulas:

$$LE\ (\%) = {}^{m(PMB\ in\ PBN)}/_{m\ (PBN)} \times 100\% \quad (1)$$

where m(PBN) denotes the total mass of PBN particles and m(PMB in PBN) denotes the mass of PMB in PBN.

$$EE\ (\%) = {}^{m(PMB\ in\ PBN)}/_{m\ (PMB)} \times 100 \quad (2)$$

where m(PBN in PBN) denotes the mass of PMB in PBN, and m(PMB) denotes the total mass of PMB added in the synthesis process.

pH-Responsive Releasing Curve of Drugs: PBS with different pH values (5.5, 6.5, and 7.4, respectively) was used as the buffer medium to simulate the normal tissue environment and the acidic microenvironment of bacterial infection. The PBN was placed in a dialysis bag with a molecular weight cut-off of 3500 Da, which was then placed in a centrifuge tube with buffer medium and shaken gently at 37°C. At a predetermined fixed time point, 1 mL of extradialysis fluid was removed from the centrifuge tube and immediately replenished with the same volume of fresh PBS buffer solution. The absorbance of the withdrawn extradialysis solution was measured by ultraviolet spectrophotometer, and the absorbance was converted into drug concentration according to the standard curve previously established, so as to plot the drug release curve of PMB/BF in different simulated environments.

The Measurement of MIC and MBC: Multi-drug-resistant *S. aureus* (MDR-SA) and *P. aeruginosa* (MDR-PA) were selected as model pathogens for in vitro antibacterial evaluation. Single colonies of each strain were aseptically transferred into Tryptone Soy Broth (TSB) and incubated under standardized conditions (37°C, 180 rpm) for 8 h to achieve logarithmic-phase bacterial suspensions (1×10^6 CFU mL^{-1}).

The antibacterial efficacy of the synthesized nanodrug (PBN) was quantified via determination of the Minimum Inhibitory Concentration (MIC). Four experimental groups were established: 1) PMB monotherapy, 2) BF monotherapy, 3) a physical mixture of PMB and BF (PMB/BF), and 4) the PBN complex. The PMB/BF group was formulated to maintain stoichiometric equivalence to the PBN composition (physical mixing). Serial dilutions of each treatment were prepared, and 100 µL aliquots of diluted agents were co-incubated with 100 µL bacterial suspensions (1×10^6 CFU mL^{-1}) in 96-well plates (Nest, Jiangsu, China) for 24 h at 37°C. Bacterial growth inhibition was assessed via microplate reader (OD_{6nnnm}, PerkinElmer, USA), with the MIC defined as the lowest drug concentration yielding ≥90% growth suppression relative to untreated controls ($N = 3$).

Minimum Bactericidal Concentration (MBC) determination was performed using a colony enumeration protocol. Post-incubation bacterial suspensions from MIC assays were serially diluted, and 100 µL aliquots were plated onto Tryptone Soy Agar (TSA). Plates were incubated at 37°C for 24 h, after which viable colonies were enumerated. The MBC was defined as the lowest drug concentration resulting in ≤5 CFU per plate, corresponding to ≥99.9% bactericidal activity ($N = 3$).

Influence by CCCP Co-Incubation: To investigate energy-dependent antibacterial mechanisms, bacterial suspensions were pre-incubated with the protonophore inhibitor carbonyl cyanide m-chlorophenylhydrazone (CCCP; 2 µg mL^{-1}) for 10 min to dissipate transmembrane proton gradients. Post-treatment, samples were subjected to centrifugation (8,000 × g, 3 min; 7500 rpm equivalent) for cellular pelleting, followed by supernatant removal. Pelleted biomass was resuspended in sterile TSB or isotonic saline (0.9% NaCl) to generate CCCP-treated experimental cohorts and untreated controls. For comparative antibacterial assessment, equimolar concentrations of the nanotherapeutic PBN were introduced to both CCCP-compromised and untreated bacterial suspensions. Reaction systems were maintained at 37°C under orbital agitation (200 rpm) for 8 h to simulate physiological conditions. Post-incubation, bacterial viability was quantified via a standardized serial dilution protocol. Briefly, cultures were serially diluted in sterile PBS, and 100 µL aliquots were plated onto TSA using a quantitative spread-plate technique. Plates were aerobically in-

cubated at 37°C for 24 h, after which CFU were enumerated. Bactericidal efficacy was calculated as $\log_{1n}$ reduction in CFU/mL relative to untreated controls ($N = 3$).

Measurement of Bacterial Surface Charge: The PBN solution was mixed with the bacterial suspension (bacterial concentration of 1×10^9 CFU mL^{-1}) and co-cultivated for 2 h (37°C, 200 rpm). Then, the mixture containing bacteria was transferred to a centrifuge tube and centrifuged at 7500 rpm for 3 min. The supernatant was discarded, and the precipitated bacteria were resuspended in deionized water, after which the surface charge of the bacteria was measured by DLS.

Bacterial Morphology Detection: PMB, BF, PMB/BF, and PBN drugs were co-cultured with bacterial suspension (1×10^9 CFU mL^{-1}) for 6 h. After the incubation, the mixture containing bacteria was transferred to a centrifuge tube and centrifuged at 7500 rpm for 3 min to precipitate the bacteria. After the supernatant was discarded, 2.5% glutaraldehyde solution was added to the precipitated bacteria to immobilize the bacteria for 2 h. After fixation, the samples were dehydrated with different concentrations of ethanol solution (30%, 50%, 60%, 70%, 80%, 90%, 100%) in a gradient, and then the morphology of the bacteria was observed and recorded by scanning electron microscope (SEM), in order to analyze the effects of different drug treatments on the morphology and structure of the bacteria.[37]

Protein Leakage Measurement: The PMB, BF, PMB/BF, and PBN drugs were incubated with the bacterial suspension (1×10^9 CFU mL^{-1}) for 6 h. After incubation, 20 µL aliquots were aseptically collected from each treatment group and combined with 200 µL of bicinchoninic acid (BCA) protein assay working solution. Reaction mixtures were incubated at 37°C for 1 h to facilitate chromogenic development. Absorbance measurements were performed spectrophotometrically at 562 nm. Protein concentrations were interpolated from a pre-established bovine serum albumin (BSA) standard curve ($R^2 \geq 0.995$), enabling quantitative determination of cytoplasmic protein release.[38] The positive control, representing maximal protein liberation via complete membrane disruption, and the negative control, reflecting baseline autolytic activity, served as critical reference points for normalizing experimental data ($N = 3$).

Membrane Polarization Assay: Bacterial suspensions (1×10^9 CFU mL^{-1}) were co-incubated with PMB, BF, PMB/BF, and PBN for 4 h at 37°C under aerobic conditions. Post-incubation, 100 µL aliquots of each treatment group were combined with 10 µL of 3,3′-diethyloxacarbocyanine iodide ($DiOC_2(3)$, 30 µM) and incubated in light-protected conditions at ambient temperature (25°C) for 15–20 min to facilitate dye internalization and membrane potential-dependent staining.[39] Fluorescence quantification was performed using a fluorescence microplate reader (PerkinElmer, USA) calibrated for the cyanine dye spectrum, with excitation and emission wavelengths set to 482 and 497 nm, respectively. Signal intensities were normalized to untreated bacterial controls to account for background fluorescence ($N = 3$).

Membrane Permeability Assay: The drugs in each group of PMB, BF, PMB/BF, and PBN were co-cultured with bacterial suspension (1×10^9 CFU mL^{-1}) at 37°C and 180 rpm for 1 h. Bacteria were centrifuged (7500 rpm, 3 min) and re-suspended in 2-nitrophenyl-β-D-galactopyranoside solution (0.015 g mL^{-1}) for 3 h. After that, the bacterial were centrifuged (7500 After that, the bacteria were centrifuged (7500 rpm, 3 min) and the supernatant was aspirated to determine the OD value at 420 nm.[40]

Bacterial Growth Kinetics Analysis: Bacterial growth dynamics were observed by determining the bacterial growth curves. Different concentrations of PMB, BF, PMB/BF, PBN dilutions were co-cultured with the mixed bacterial suspensions, and the samples were continuously sampled at intervals of 1 h. After each sample was taken, the absorbance at OD_{600} was determined to plot the growth curve of the mixed bacteria, and the corresponding concentrations of PMB, BF, and PMB/BF were formulated to mirror the stoichiometric composition of PBN ($N = 3$).

Establishment and Therapeutic Evaluation of a Mixed-Bacteria Wound Infection Model In Mice: Female BALB/c mice (18–20 g; 7–8 weeks old) were procured from Beijing Viton Lihua Laboratory Animal Science and Technology Co. The experimental protocol received approval from the SPF Animal Section of China-Japan Friendship Hospital (approval number: 035389). A mixed bacterial suspension was prepared by combining MDR-SA and MDR-PA at a concentration of 1×10^9 CFU mL^{-1} in a 1:1 volume ratio. The mice were randomly divided into 5 groups ($N = 3$). Following anesthesia and hair removal from the dorsal region, a circular full-thickness skin wound (1 cm diameter) was created using a circular perforator. Subsequently, 50 µL of the MDR(PA/SA) suspension was applied to the wound, which was then covered with a sterile transparent dressing to facilitate a 24-h bacterial infection period, thereby establishing a mixed bacterial infection model. Daily treatments were administered via in situ injection of PBS, PMB, BF, PMB/BF, and PBN. Throughout the treatment period, mice were monitored daily for body weight, and wound progression was documented through observation and photography. Upon completion of the treatment regimen, blood samples were collected for serum inflammatory factor analysis. Skin tissues underwent hematoxylin-eosin (H&E) and Masson staining, and were homogenized to quantify residual bacterial counts in the wounds. Additionally, major organs—including the heart, liver, spleen, lungs, and kidneys—were subjected to H&E staining to assess biosafety ($N = 3$).

In Vitro Cytotoxicity Assay: The cytotoxicity of the compounds was evaluated using the MTT assay on RAW264.7 macrophages and L929 fibroblasts.[41] Cells were seeded into 96-well plates at a density of 8×10^3 cells per well and incubated overnight to allow for adherence. Subsequently, cells were treated with varying concentrations of the test compounds (final concentrations: 1, 2, 3, 4, 8, 16, 32, 64, and 128 µg mL^{-1}) for 24 h. Following treatment, 10 µL of MTT solution was added to each well, and the plates were incubated for an additional 4 h under light-protected conditions. After incubation, 100 µL of 10% SDS solution was added to each well to solubilize the formazan crystals formed. The absorbance at 570 nm was then measured using a microplate reader to determine the relative cell viability. This protocol aligns with standard MTT assay procedures, which measure the reduction of MTT to insoluble formazan by mitochondrial dehydrogenases in living cells, serving as an indicator of cell viability ($N = 3$).

Hemolysis Assay: The hemolysis assay was conducted using fresh mouse blood. Initially, 1 mL of anticoagulated whole blood was diluted with 2 mL PBS and centrifuged at 500 g for 10 min. The supernatant was discarded, and the erythrocytes were washed three times with PBS to remove plasma and leukocytes, ensuring a standardized erythrocyte suspension. The final erythrocyte suspension was adjusted to a total volume of 10 mL with PBS. For the hemolysis assay, 0.8 mL of each drug formulation was incubated with 0.2 mL of the prepared erythrocyte suspension at 37°C with gentle agitation at 30 rpm for 3 h. Following incubation, the mixtures were centrifuged at 10,000 g for 5 min to pellet intact erythrocytes. A 100 µL aliquot of the resulting supernatant from each sample was transferred to a 96-well plate, and the absorbance was measured at 540 nm using a microplate reader to quantify the extent of hemolysis. Deionized water served as the positive control, representing 100% hemolysis, while PBS was used as the negative control, indicating 0% hemolysis. The percentage of hemolysis induced by each drug formulation was calculated relative to these controls.

Hemolysis rate was calculated as follows:

$$Hemolysis\ Rate\ (\%) = {}^{Abs(drug)-Abs(PBS)}/_{Abs\,(DI\,water)\,-\,Abs\,(PBS)} \times 100\% \quad (3)$$

where Abs(drug) is the OD value after co-incubation of different concentrations of drug and erythrocyte suspension; Abs(PBS) is the OD value after co-incubation of PBS and erythrocyte suspension; DI water is the OD value after co-incubation of DI water and erythrocyte suspension.

Data Statistical Analysis: Statistical analysis was performed in GraphPad Prism (GraphPad Software, USA). Quantitative data were expressed as mean ± standard deviation (SD). Statistically significant differences (p) were analyzed by Student's t-test or one-way ANOVA with a Tukey test. **** $p < 0.0001$, *** $p < 0.001$, ** $p < 0.01$, * $p < 0.05$, ns $p > 0.05$.

Supporting Information

Supporting Information is available from the Wiley Online Library or from the author.

Acknowledgements

This research was supported by the National Natural Science Foundation of China (52273118, 22275013), the Beijing Municipal Natural Science Foundation (2254093), and the Fundamental Research Funds for the Central Universities (buctrc202419).

Conflict of Interest

The authors declare no conflict of interest.

Author Contributions

J.Y. and X.Z. contributed equally to this work. J.Y. and X.Z. designed, developed, and organized the study, wrote-reviewed and edited the manuscript. Y.F. provided assistance for materials preparation and measurement. G.L., W.X., and X.W. designed, guided, and funded the study, wrote-reviewed and edited the manuscript. All authors have approved the final version of the manuscript.

Data Availability Statement

The data that support the findings of this study are available from the corresponding author upon reasonable request.

Keywords

bacterial mixed infection, carrier-free nanodrug, Gram-negative bacteria, Gram-positive bacteria, synergistic antibacterial

Received: April 13, 2025
Revised: July 25, 2025
Published online:

[1] R. Teng, Y. Yang, Z. Zhang, K. Yang, M. Sun, C. Li, Z. Fan, J. In Du, *Adv. Funct. Mater.* **2023**, *33*, 2214454.
[2] K. S. Kim, *Nat. Rev. Neurosci.* **2003**, *4*, 376.
[3] M. Yin, J. Wu, M. Deng, P. Wang, G. Ji, M. Wang, C. Zhou, N. T. Blum, W. Zhang, H. Shi, N. Jia, X. Wang, P. Huang, *ACS Nano* **2021**, *15*, 17842.
[4] L. J. Sherrard, M. M. Tunney, J. S. Elborn, *Lancet* **2014**, *384*, 703.
[5] M. Vallet-Regí, D. Lozano, B. González, I. Izquierdo-Barba, *Adv. Healthcare. Mater.* **2020**, *9*, 2000310.
[6] M. K. Kim, Q. Chen, A. Echterhof, N. Pennetzdorfer, R. C. McBride, N. Banaei, E. B. Burgener, C. E. Milla, P. L. Bollyky, *Nat. Commun.* **2024**, *15*, 9987
[7] Y. Zhao, Q. Guo, X. Dai, X. Wei, Y. Yu, X. Chen, C. Li, Z. Cao, X. Zhang, *Adv. Mater.* **2019**, *31*, 1806024.
[8] M. Igo, L. Xu, A. Krishna, S. Stewart, L. Xu, Z. Li, J. L. Weaver, H. Stone, L. Sacks, T. Bensman, J. Florian, R. Rouse, X. Han, *Gut Microbes* **2023**, *15*, 2271150.
[9] S. Hajebi, S. Yousefiasl, I. Rahimmanesh, A. Dahim, S. Ahmadi, F. B. Kadumudi, N. Rahgozar, S. Amani, A. Kumar, E. Kamrani, M. Rabiee, A. Borzacchiello, X. Wang, N. Rabiee, A. Dolatshahi-Pirouz, P. Makvandi, *Adv. Healthcare. Mater.* **2022**, *11*, 2201583.
[10] C. J. L. Murray, K. S. Ikuta, F. Sharara, L. Swetschinski, G. Robles Aguilar, A. Gray, C. Han, C. Bisignano, P. Rao, E. Wool, S. C. Johnson, A. J. Browne, M. G. Chipeta, F. Fell, S. Hackett, G. Haines-Woodhouse, B. H. Kashef Hamadani, E. A. P. Kumaran, B. McManigal, S. Achalapong, R. Agarwal, S. Akech, S. Albertson, J. Amuasi, J. Andrews, A. Aravkin, E. Ashley, F.-X. Babin, F. Bailey, S. Baker, et al., *The Lancet* **2022**, *399*, 629
[11] B. Li, A. L. Armstead, *Int. J. Nanomed.* **2011**, *6*, 3281.
[12] M. Zhou, Y. Qian, J. Xie, W. Zhang, W. Jiang, X. Xiao, S. Chen, C. Dai, Z. Cong, Z. Ji, N. Shao, L. Liu, Y. Wu, R. Liu, *Angew. Chem. Int. Ed.* **2020**, *59*, 6294.
[13] W.-H. Chen, Q.-W. Chen, Q. Chen, C. Cui, S. Duan, Y. Kang, Y. Liu, Y. Liu, W. Muhammad, S. Shao, C. Tang, J. Wang, L. Wang, M.-H. Xiong, L. Yin, K. Zhang, Z. Zhang, X. Zhen, J. Feng, C. Gao, Z. Gu, C. He, J. Ji, X. Jiang, W. Liu, Z. Liu, H. Peng, Y. Shen, L. Shi, X. Sun, et al., *Sci. China Chem.* **2022**, *65*, 1010.
[14] X. Kang, F. Bu, W. Feng, F. Liu, X. Yang, H. Li, Y. Yu, G. Li, H. Xiao, X. Wang, *Adv. Mater.* **2022**, *34*, 2206765.
[15] W. Feng, G. Li, X. Kang, R. Wang, F. Liu, D. Zhao, H. Li, F. Bu, Y. Yu, T. F. Moriarty, Q. Ren, X. Wang, *Adv. Mater.* **2022**, *34*, 2109789.
[16] W. Feng, M. Chittò, W. Xie, Q. Ren, F. Liu, X. Kang, D. Zhao, G. Li, T. F. Moriarty, X. Wang, *ACS Nano* **2024**, *18*, 8017.
[17] H. Li, W. Zang, Z. Mi, J. Li, L. Wang, D. Xie, L. Zhao, D. Wang, *J. Controlled Release* **2022**, *352*, 256.
[18] Y. Guo, K. Jiang, Z. Shen, G. Zheng, L. Fan, R. Zhao, J. Shao, *ACS Appl. Mater. Interfaces* **2017**, *9*, 43508.
[19] H. Sun, M. Sun, Y. You, J. Xie, X. Xu, J. Li, *Chem. Eng. J.* **2023**, *471*, 144597.
[20] L. Yang, C. Zhan, X. Huang, L. Hong, L. Fang, W. Wang, J. Su, *Adv. Healthcare. Mater.* **2020**, *9*, 2000186.
[21] M. Z. Doymaz, E. Karaaslan, *Infect. Dis.* **2019**, *51*, 676.
[22] Y. Tian, Y. Cao, Y. Wang, W. Yang, J. Feng, *Adv. Mater.* **2013**, *25*, 2980.
[23] R. Fernandes, N. R. Smyth, O. L. Muskens, S. Nitti, A. Heuer-Jungemann, M. R. Ardern-Jones, A. G. Kanaras, *Small* **2015**, *11*, 713.
[24] F. Yu, C. Chen, G. Yang, Z. Ren, H. Cao, L. Zhang, W. Zhang, *Sci. China Chem.* **2021**, *64*, 459.
[25] X. Yuan, Y. Zhou, Y. Wang, L. Liu, G. Yang, *Carbohydr. Polym.* **2024**, *326*, 121619.
[26] L. Unterholzner, *Cell* **2023**, *186*, 3145.
[27] K. R. Allison, M. P. Brynildsen, J. J. Collins, *Nature* **2011**, *473*, 216.
[28] S. R. Naganathan, M. Popović, A. C. Oates, *Nature* **2022**, *605*, 516.
[29] D. M. Needham, C. Poirier, C. Bachy, E. E. George, S. Wilken, C. C. M. Yung, A. J. Limardo, M. Morando, L. Sudek, R. R. Malmstrom, P. J. Keeling, A. E. Santoro, A. Z. Worden, *Nat. Microbiol.* **2022**, *7*, 1466.
[30] S. Shibata, M. Shoji, K. Okada, H. Matsunami, M. M. Matthews, K. Imada, K. Nakayama, M. Wolf, *Nat. Microbiol.* **2020**, *5*, 830.
[31] F. Liu, L. Zou, Y. Chen, Z. Liu, Y. Huang, Q. Jin, J. Ji, *Nano Res.* **2024**, *17*, 8325.
[32] H. W. Taber, J. P. Mueller, P. F. Miller, A. S. Arrow, *Microbiol Rev.* **1987**, *51*, 439.
[33] M. A. Farha, C. P. Verschoor, D. Bowdish, E. D. Brown, *Chem. Biol.* **2013**, *20*, 1168.
[34] T. M. Chicano, L. Dietrich, N. M. De Almeida, M. Akram, E. Hartmann, F. Leidreiter, D. Leopoldus, M. Mueller, R. Sánchez, G. H. L. Nuijten, J. Reimann, K.-A. Seifert, I. Schlichting, L. Van Niftrik, M. S. M. Jetten, A. Dietl, B. Kartal, K. Parey, T. R. M Barends, *Nat. Microbiol.* **2021**, *6*, 1129.
[35] L. Poirel, A. Jayol, P. Nordmann, *Clin. Microbiol. Rev.* **2017**, *30*, 557.
[36] H. Fan, H. Li, G. Liu, W. Cong, H. Zhao, W. Cao, J. Zheng, *J. Exp. Clin. Cancer. Res.* **2017**, *36*, 163.
[37] D. Zhao, W. Feng, X. Kang, H. Li, F. Liu, W. Zheng, G. Li, X. Wang, *J. Mater. Chem. B* **2023**, *11*, 2958.
[38] R. Wang, X. Kong, W. Zhang, W. Zhu, L. Huang, J. Wang, X. Zhang, X. Liu, N. Hu, Y. Suo, J. Wang, *Appl. Catal., B* **2018**, *225*, 228.
[39] M. Aqawi, R. V. Sionov, R. Gallily, M. Friedman, D. Steinberg, *Front. Microbiol.* **2021**, *12*, 656471.
[40] M. Zhang, Y. Yu, L. Lian, W. Li, J. Ren, Y. Liang, F. Xue, F. Tang, X. Zhu, J. Ling, J. Dai, *Probiotics. Antimicro. Prot.* **2022**, *14*, 169.
[41] L. Cheng, S. Zhang, Q. Zhang, W. Gao, S. Mu, B. Wang, *Heliyon* **2024**, *10*, 36118.